

# Elucidating the Mechanism of Iron-Catalyzed Graphitization: The First Observation of Homogeneous Solid-State Catalysis

Robert D. Hunter, Masaki Takeguchi, Ayako Hashimoto, Kannan M. Ridings, Shaun C. Hendy, Dmitri Zakharov, Nils Warnken, Jack Isaacs, Sol Fernandez-Muñoz, Joaquín Ramirez-Rico,\* and Zoe Schnepf\*

Dedication: In the memory of Professor Roy L. Johnston

Carbon is a critical material for existing and emerging energy applications and there is considerable global effort in generating sustainable carbons. A particularly promising area is iron-catalyzed graphitization, which is the conversion of organic matter to graphitic carbon nanostructures by an iron catalyst. In this paper, it is reported that iron-catalyzed graphitization occurs via a new type of mechanism that is called homogeneous solid-state catalysis. Dark field in situ transmission electron microscopy is used to demonstrate that crystalline iron nanoparticles “burrow” through amorphous carbon to generate multiwalled graphitic nanotubes. The process is remarkably fast, particularly given the solid phase of the catalyst, and in situ synchrotron X-ray diffraction is used to demonstrate that graphitization is complete within a few minutes.

## 1. Introduction

In chemical and biochemical processes, catalysts are typically defined as homogeneous or heterogeneous. Homogeneous catalysts are molecular species that drive reactions of other molecular species in the gas or liquid phase. In contrast, heterogeneous catalysis involves the reaction of liquid, solution, or vapor

phase molecular species at a solid catalyst surface. In the realm of materials science, the concept of catalysis expands to include growth of solid materials from nanoparticles. Here, precursor species dissolve in a liquid or solid nanoparticle and a new material grows from the nanoparticle, typically in the form of a nanowire or nanotube. The function of the catalyst is to provide a surface for nucleation of the 1D nanostructure and to facilitate diffusion of atoms from the precursor to the growing material surface. Catalytic growth is used widely in research and industry to produce metal, chalcogenide and oxide nanowires,<sup>[1]</sup> and carbon nanotubes.<sup>[2]</sup> This type of catalytic outgrowth is called vapor–liquid–solid (Figure 1a), vapor–solid–solid, solution–liquid–solid, solution–solid–solid, or solid–liquid–solid (Figure 1b) growth, depending on the physical phase of the precursors, catalyst, and product, respectively.<sup>[3]</sup>

Whatever the type of catalyst, there is a need for movement. Reactants need to diffuse to the active site on homogeneous or heterogeneous catalysts and products need to move away. In the case of 1D nanostructure growth, precursors need to be transported to

R. D. Hunter, J. Isaacs, Z. Schnepf  
School of Chemistry  
University of Birmingham  
Birmingham B152TT, UK  
E-mail: [z.schnepf@bham.ac.uk](mailto:z.schnepf@bham.ac.uk)

M. Takeguchi, A. Hashimoto  
Center for Basic Research on Materials  
National Institute for Materials Science  
Tsukuba, Ibaraki 305-0047, Japan

K. M. Ridings, S. C. Hendy  
Department of Physics  
The University of Auckland  
Auckland 1010, New Zealand

D. Zakharov  
Center for Functional Nanomaterials  
Brookhaven National Laboratory  
Upton, NY 11973-5000, USA

N. Warnken  
School of Metallurgy and Materials  
University of Birmingham  
Birmingham B152TT, UK

S. Fernandez-Muñoz, J. Ramirez-Rico  
Instituto de Ciencia de Materiales de Sevilla (ICMS)  
Universidad de Sevilla-CSIC  
Sevilla 41092, Spain  
E-mail: [jrr@us.es](mailto:jrr@us.es)

 The ORCID identification number(s) for the author(s) of this article can be found under <https://doi.org/10.1002/adma.202404170>

© 2024 The Author(s). Advanced Materials published by Wiley-VCH GmbH. This is an open access article under the terms of the [Creative Commons Attribution](#) License, which permits use, distribution and reproduction in any medium, provided the original work is properly cited.

DOI: 10.1002/adma.202404170

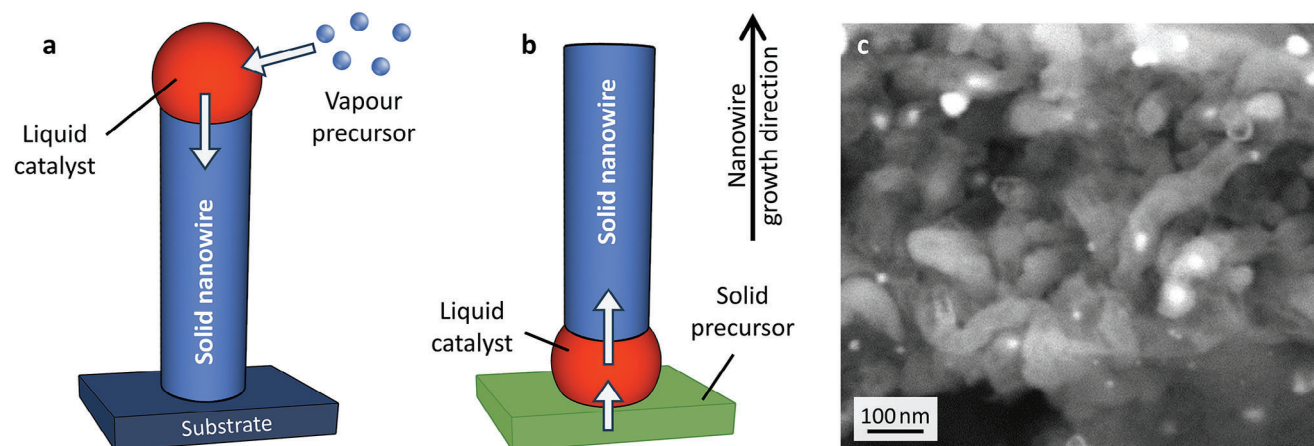


**Figure 1.** Schematic of a) vapor–liquid–solid and b) solid–liquid–solid catalytic growth of 1D nanostructures with arrows showing the direction of transport of atoms. c) Scanning electron microscope (SEM) image of nanotubes formed from pyrolysis of cellulose with iron nitrate (reproduced with permission from reference 5).

the catalyst interface, atoms need to diffuse through the catalyst, and the nanowire or nanotube needs to grow out from the catalyst. Because of the multiple transport mechanisms required, it is reasonable to assume that at least one phase in a catalytic process must be a liquid or gas. In this paper, we demonstrate the first catalytic system where the precursor, catalyst and product are all solids.

The system in question is catalytic graphitization.<sup>[4]</sup> When organic matter (e.g., biomass or biopolymers) is mixed with iron salts and heated in an inert atmosphere, the organic molecules decompose into amorphous carbon and the iron salts form iron or iron carbide ( $\text{Fe}_3\text{C}$ ) nanoparticles. On further heating ( $\approx 700\text{--}800^\circ\text{C}$ ), the catalytic nanoparticles convert the amorphous carbon matrix to a dense network of nanotubes made up of layered graphene sheets (Figure 1c).<sup>[5]</sup> These are analogous to multiwalled carbon nanotubes but are irregular in shape. Fracture planes of graphitized biomass show that the nanotubes penetrate through the sample, indicating that the catalyst particles travel through the whole amorphous carbon matrix. Transmission electron microscopy (TEM) has been used to show that the catalyst particles move along irregular pathways through the amorphous carbon, leaving a graphitic nanotube trail behind them.<sup>[6]</sup> The fast movement and liquid-like appearance of the catalyst particles have led many authors, including ourselves, to assume that the catalyst is in the liquid state.<sup>[7–10]</sup> We now report that graphitization actually occurs via rapid diffusion of a crystalline catalyst particle through a solid amorphous carbon matrix. This detailed insight into the mechanism of graphitization will enable much better understanding and prediction of structure–property relationships in carbons from catalytic graphitization.

## 2. Results and Discussion

### 2.1. In Situ Transmission Electron Microscopy

Iron-doped amorphous carbon powder (prepared from iron nitrate and cellulose) was heated to  $900^\circ\text{C}$  in a transmission electron microscope (TEM). Video footage at  $800^\circ\text{C}$  (Video S1, Sup-

porting Information; and Figure 2a) shows that the graphitization process is characterized by rapid movement of liquid-like particles through the amorphous carbon matrix. The movement is irregular, with particles continuously stopping and starting, and the average speed was estimated as  $4\text{ nm s}^{-1}$ . The particles travel along irregular pathways and closely follow the edge of the carbon sample, showing no evidence of outgrowth from the carbon surface. As the particles move, they dissolve amorphous carbon from the matrix and deposit trails of graphitized carbon in the form of nanotubes (Video S2, Supporting Information; and Figure 2b,c). The nanotubes are irregularly shaped with walls made up of stacked layers of straight or curved graphene sheets, (Figure 2d). During continued heating, the particle movement becomes more sporadic. Particles appear to stop moving when they have exhausted their supply of amorphous carbon and become surrounded by graphitic material. A helpful analogy for this is the old mobile phone game of snake, where the head of the snake can become trapped in coils of its own body (Figure 2e). Many particles continue to show liquid-like behavior after their fast movement stops and can be seen to move slightly within the cavity they are trapped in (Figure 2f). Selected area electron diffraction and high-resolution imaging of particles that had stopped moving showed patterns characteristic of crystalline iron (Figure S1, Supporting Information) or iron carbide (Figure S2, Supporting Information).

Dark field TEM footage was collected by selecting diffraction spots using the objective aperture and using electrons diffracted along that angle to generate images.<sup>[11]</sup> This method is used to show bright contrast only for crystalline particles that are diffracting electrons along the selected angle range. The dark field TEM video footage of this sample (Video S3, Supporting Information) shows that fast moving catalyst particles alternate between bright and dark as they move (Figure 3a). The observation of particles remaining continuously bright for sections of movement through the carbon matrix (Figure 3b) confirms that the particles are crystalline, while they are catalyzing graphitization. The alternating between bright and dark indicates that the particles are changing crystallographic orientation as they move. It could be argued

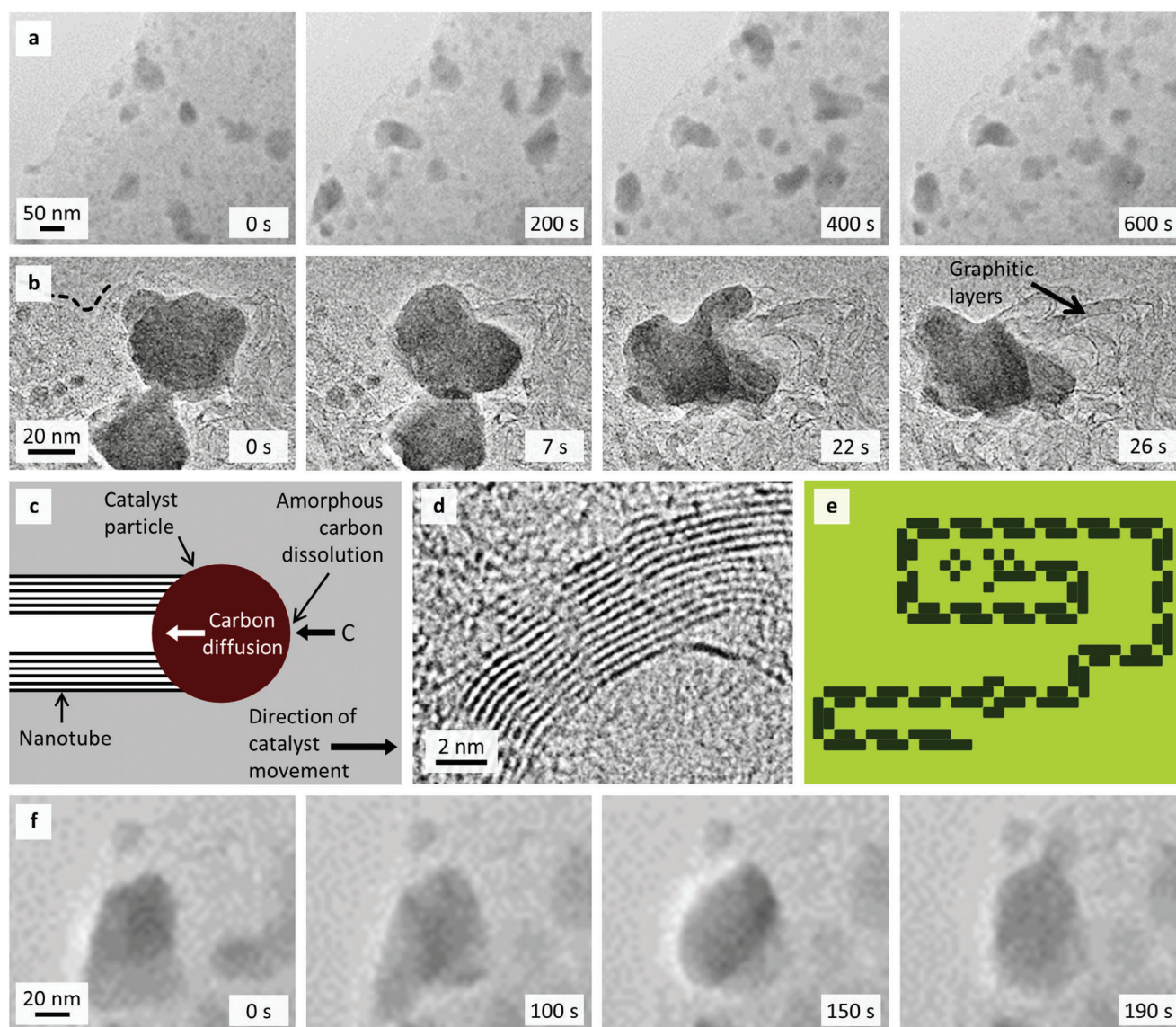


**Figure 2.** a) Sequence images from TEM video at 800 °C showing catalyst particles moving rapidly through an amorphous carbon matrix. b) Images from a video at higher magnification showing a single catalyst particle generating a multiwalled graphitic nanotube (dashed line indicates the edge of the amorphous carbon). c) Schematic of catalyst particle movement with dissolution of amorphous carbon at the front edge of the catalyst and deposition of a graphitic nanotube at the back edge. d) TEM image showing the multiple graphitic walls of a nanotube. e) Schematic of the mobile phone game “snake” showing the snake becoming trapped. f) Images from TEM video of a catalyst particle that has become trapped but continues to move slightly.

that the dark/bright alternation is a result of sequential melting and solidification. However, this would be energetically a lot less favorable than particle rotation as it would involve consumption and release of latent heat. Crystalline grains are known to rotate readily in polycrystalline systems during deformation and annealing.<sup>[12]</sup> Similarly, Wang et al. observed that Co-W-C alloy catalyst particles would rotate during the formation of carbon nanotubes from a  $C_2H_4$  feedstock and were able to measure the changes in orientation of the catalyst nanoparticles.<sup>[13]</sup> However, in this work, the rotation of the catalyst particles appears to be extremely fast, making it challenging to quantify in the same manner.

## 2.2. In Situ Synchrotron X-Ray Diffraction

In situ synchrotron X-ray diffraction (XRD) data supports the in situ TEM observations. Iron-doped amorphous carbon was prepared from cellulose and  $Fe(NO_3)_3$  and heated to 400 °C in  $N_2$  to remove volatile organic pyrolysis products. The sample was then heated under  $N_2$  at 5 °C min<sup>-1</sup> to 800 °C in the synchrotron beam. Heat maps of the diffraction data (Figure S3, Supporting Information) show the appearance of very broad peaks for iron oxide. The broad nature of the peaks makes refinement difficult but the sudden appearance of the peaks at 600 °C suggests they are caused by carbothermal reduction of  $Fe_3O_4$  to  $FeO_x$  (wustite).<sup>[14]</sup>



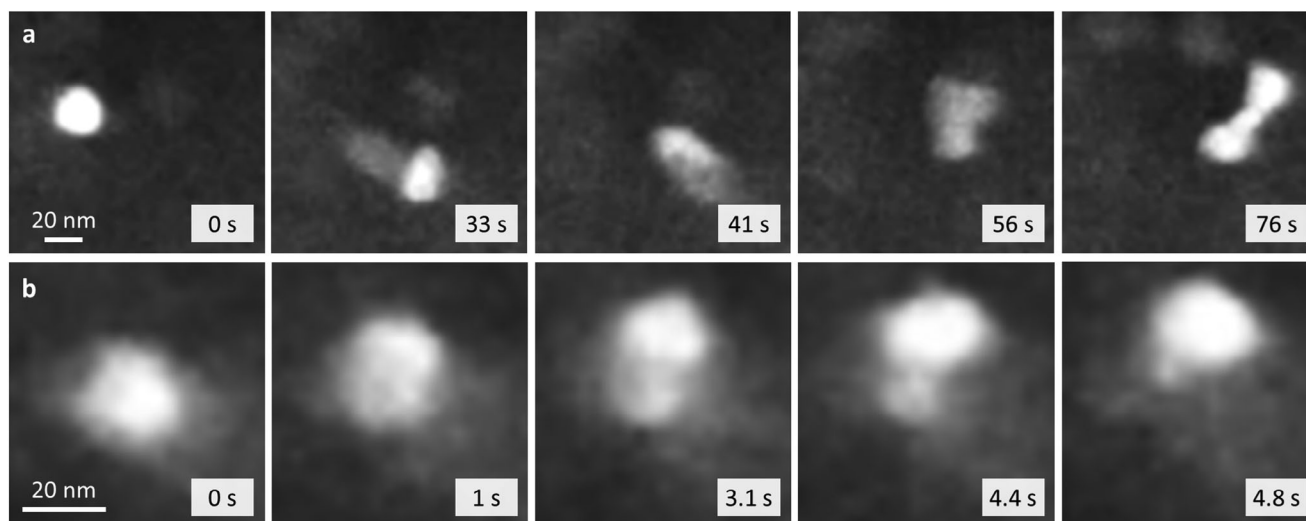


**Figure 3.** a) Images from dark field TEM video at 900 °C showing a catalyst particle moving through the amorphous carbon matrix and alternating between dark and bright appearance. b) Images from dark field TEM showing a particle remaining bright for a section of movement, proving that the catalyst is crystalline during movement.

An expanded section of the heat map (**Figure 4a**) shows that sharp peaks for Fe/Fe<sub>3</sub>C emerge around 750 °C. A peak corresponding to the interplanar spacing of graphitic carbon ( $Q = 1.8 \text{ \AA}^{-1}$ ) evolves alongside the Fe/Fe<sub>3</sub>C peaks (**Figure 4b**), indicating that graphitization commences immediately after forma-

tion of the catalyst. A plot of normalized graphite peak intensity (**Figure 4c**) shows that graphitization is largely complete within 10 min. This confirms that the in situ TEM observations of fast catalyst movement are consistent with the bulk behavior of the system.

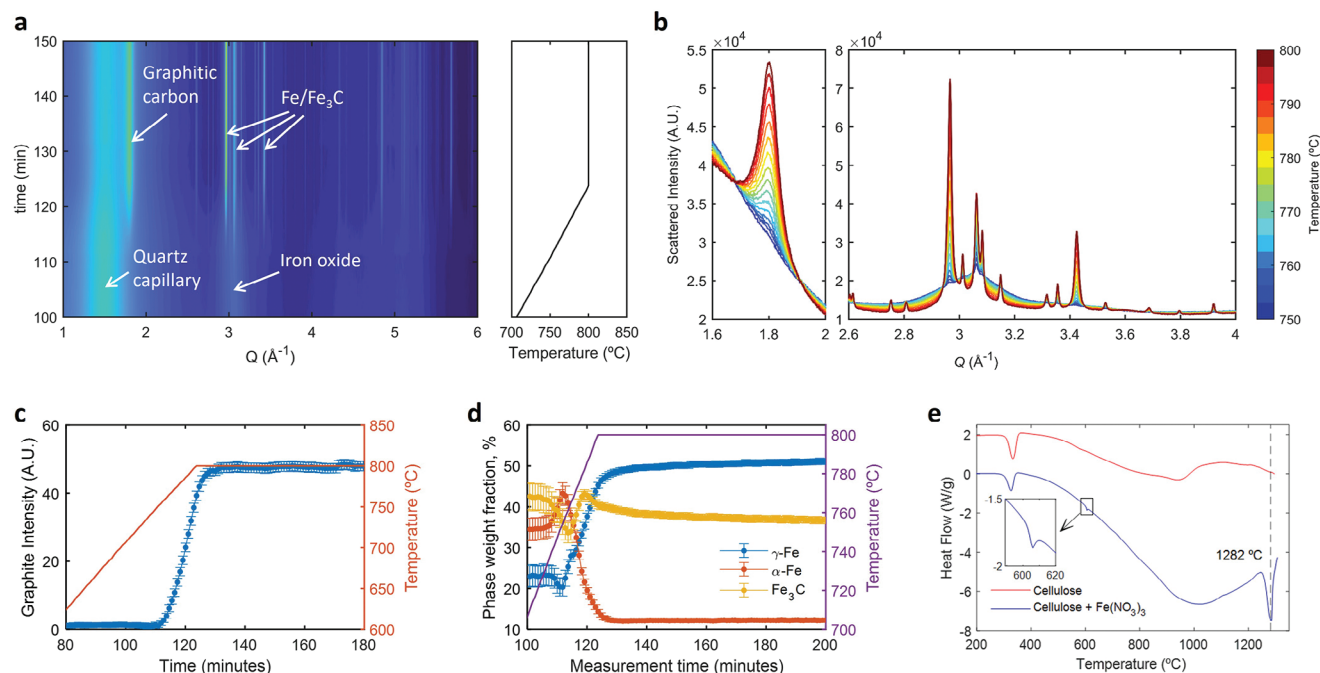


**Figure 4.** a) Heatmap showing diffracted intensity as a function of scattering vector magnitude  $Q$  and measurement time for in situ diffraction measurements in the range  $\approx 700\text{--}800$  °C. The right panel shows the temperature program used for the experiment. b) Scattered intensity recorded at different temperatures during in situ synchrotron X-ray diffraction showing evolution of the (002) graphitic peak (left panel) and Fe-containing phases (right panel). c) Normalized graphite peak intensity and d) mass fraction of  $\alpha$ -Fe,  $\gamma$ -Fe, and Fe<sub>3</sub>C obtained from Rietveld refinement of diffraction data as a function of measurement time and plotted alongside reaction temperature. e) Differential scanning calorimetry data from bare cellulose fibers (red line) and cellulose fibers impregnated with Fe(NO<sub>3</sub>)<sub>3</sub> solution (blue line). The inset shows a small endothermic peak at  $\approx 605$  °C due to carbothermal reduction of the oxide nanoparticles.

Rietveld refinement was used to calculate phase compositions for iron-containing crystalline phases as a function of temperature. Three crystalline phases were considered for the refinement:  $\text{Fe}_3\text{C}$  (cementite),  $\alpha\text{-Fe}$  (ferrite), and  $\gamma\text{-Fe}$  (austenite). It is important to understand that weight fractions are calculated by determining the relative contribution (scale factor) of each phase to the total diffracted intensity, normalizing to 100%, and that the absolute contribution of each phase is unknown. This means that during the early stages of graphitization and  $\text{Fe}/\text{Fe}_3\text{C}$  crystallization, the values for the scale factors are relatively low and therefore the weight fractions have large uncertainties (more details can be found in the Supporting Information). Figure S4 (Supporting Information) shows the evolution of the crystalline domain size for each phase, indicating an increase in crystallinity of all the iron-containing phases alongside the growth of the graphite peak. An example of a single refinement showing all three Fe-C phases is shown in Figure S5 (Supporting Information) and full refinement details are available in the Supporting Experimental Information. Figure 4d shows the weight fraction of each of the three iron phases during the graphitization step. At the onset of graphitization, the primary crystalline phase is  $\alpha$ -iron. During graphitization, this phase largely disappears, with  $\gamma$ -iron becoming dominant and  $\text{Fe}_3\text{C}$  (cementite) also increasing. This is consistent with the phase diagram for iron/carbon.<sup>[15]</sup> The complex mixture of phases makes it impossible to conclude which is responsible for catalytic graphitization and it is possible that more than one iron phase is catalytically active for graphitization. In chemical vapor deposition (CVD) synthesis of carbon nanotubes, there is evidence that Fe and  $\text{Fe}_3\text{C}$  can both act as catalysts but for different types of carbon nanotube (straight and bamboo-like).<sup>[16]</sup> The rapid emergence of  $\gamma\text{-Fe}$  and  $\text{Fe}_3\text{C}$  alongside graphitization in the cellulose system could indicate that both phases are catalytic here.

When the sample is held at 800 °C for 2 h, the crystallographic composition stays constant (Figure S6, Supporting Information). On cooling,  $\gamma$ -iron is replaced by the lower temperature  $\alpha$ -iron phase (Figure S7, Supporting Information). This is accompanied by a small increase in the graphite peak intensity (Figure S8, Supporting Information). Carbon is more soluble in  $\gamma$ -iron than  $\alpha$ -iron,<sup>[17]</sup> so it is likely that the additional graphitic carbon is precipitated during the iron phase transformation. The fact that carbon is precipitated from the  $\gamma$ -iron phase when it transforms to the lower temperature  $\alpha$ -iron phase indicates that the  $\gamma$ -iron nanoparticles contain an appreciable amount of dissolved carbon. This supports the proposed dissolution-precipitation mechanism of graphitization.

Thermogravimetric analysis (TGA) and differential scanning calorimetry (DSC) offer further insight into the formation and nature of the active catalyst. A sample of cellulose/ $\text{Fe}(\text{NO}_3)_3$  was heated to 1350 °C under Ar. A rapid mass loss around 330 °C (Figure S9, Supporting Information) corresponds to the main decomposition step of cellulose, where carbonization of the polysaccharide releases  $\text{CO}_2$ ,  $\text{H}_2\text{O}$ , and CO. The small mass loss at 605 °C corresponds to carbothermal reduction of  $\text{Fe}_3\text{O}_4$  to  $\text{FeO}_x$ , as observed in the XRD data. This is confirmed by the release of CO and  $\text{CO}_2$  at this temperature (Figure S10, Supporting Information) and the appearance of a small endothermic peak in the DSC data (Figure 4e). The TGA/DSC data do not show the graphitization step, as this is a transformation from disor-

dered, mainly  $\text{sp}^3$ -hybridised carbon to ordered  $\text{sp}^2$ -hybridized graphitic carbon. The absence of a melting transition in the DSC data at the graphitization step provides further evidence for the bulk catalyst being solid during graphitization. Further heating of the sample reveals that the Fe-C catalyst undergoes a melting transition at 1282 °C. This is consistent with the Fe-C phase diagram, where there is a phase boundary between  $\gamma$ -iron and a liquid/ $\gamma$ -iron mixture at 1282 °C for an Fe-C alloy of  $\approx 1.3$  wt% C.<sup>[15]</sup>

### 2.3. Molecular Dynamics Simulations of the Catalyst

The observation of solid catalyst nanoparticles in our system is consistent with the bulk iron-carbon phase diagram, where liquid phases only exist above 1150 °C. However, the observed liquid-like behavior of catalysts in nanostructure growth is often rationalized with reference to the Gibbs–Thomson effect of melting point depression in nanoparticles. Therefore, we conducted simulations of Fe and Fe-C clusters to determine the effect of particle size on melting temperature. Melting of Fe nanoparticles has been modeled, but only with older potentials based on the second moment approximation of the tight binding model.<sup>[18,19]</sup> To the best of our knowledge,  $\text{Fe}_3\text{C}$  nanoparticle melting has not been modeled. Here, a classical molecular dynamics method using LAMMPS (Large-scale Atomic/Molecular Massively Parallel Simulator) was employed to study the melting behavior of free and substrate-supported iron and  $\text{Fe}_3\text{C}$  nanoparticles. Modified embedded atom model (MEAM) potentials were used to describe the Fe-Fe, Fe-C, and C-C interactions and a Lennard–Jones potential function was used to describe interactions between the nanoparticles and a structureless, mean-field substrate. Full details can be found in the Experimental Section and Supporting Information. Figure 5a shows snapshots of a heating simulation of a freestanding  $\alpha$ -iron cluster, constructed from 8393 atoms using MEAM potentials reported by Asadi et al.<sup>[20]</sup> The body-centered cubic (BCC) structure (blue atoms) breaks down with increasing temperature to give a disordered cluster (gray atoms), indicating the melting transition. Figure 5b shows caloric curves for heating and cooling of freestanding BCC iron clusters of various sizes. The heating curves show a steady shift to higher melting points with increased cluster size, as would be expected. The cooling simulations also show clear transitions corresponding to solidification. However, there is less correlation between solidification temperature and cluster size, with all solidification occurring in the 1000–1200 K temperature range. The hysteresis observed in all the simulations is due to the very fast heating and cooling rates required for molecular dynamics simulations.<sup>[21]</sup> Equilibrium melting temperatures ( $T_m$ ) for all the cluster sizes were calculated from the heating and cooling simulations (details in the Supporting Information). A plot of  $T_m$  versus  $1/\text{radius}$  (Figure 5c) shows a linear trend, consistent with Pawlow's formula<sup>[22]</sup> and with older simulations using potentials based on the second moment approximation of the tight binding model. The data indicate that a liquid iron phase could be possible below 800 °C, but only for particles that are a lot smaller ( $\approx 1$  nm diameter) than we observe in the catalytic graphitization (50–100 nm diameter). Simulations were attempted for freestanding  $\gamma$ -iron clusters but at the starting

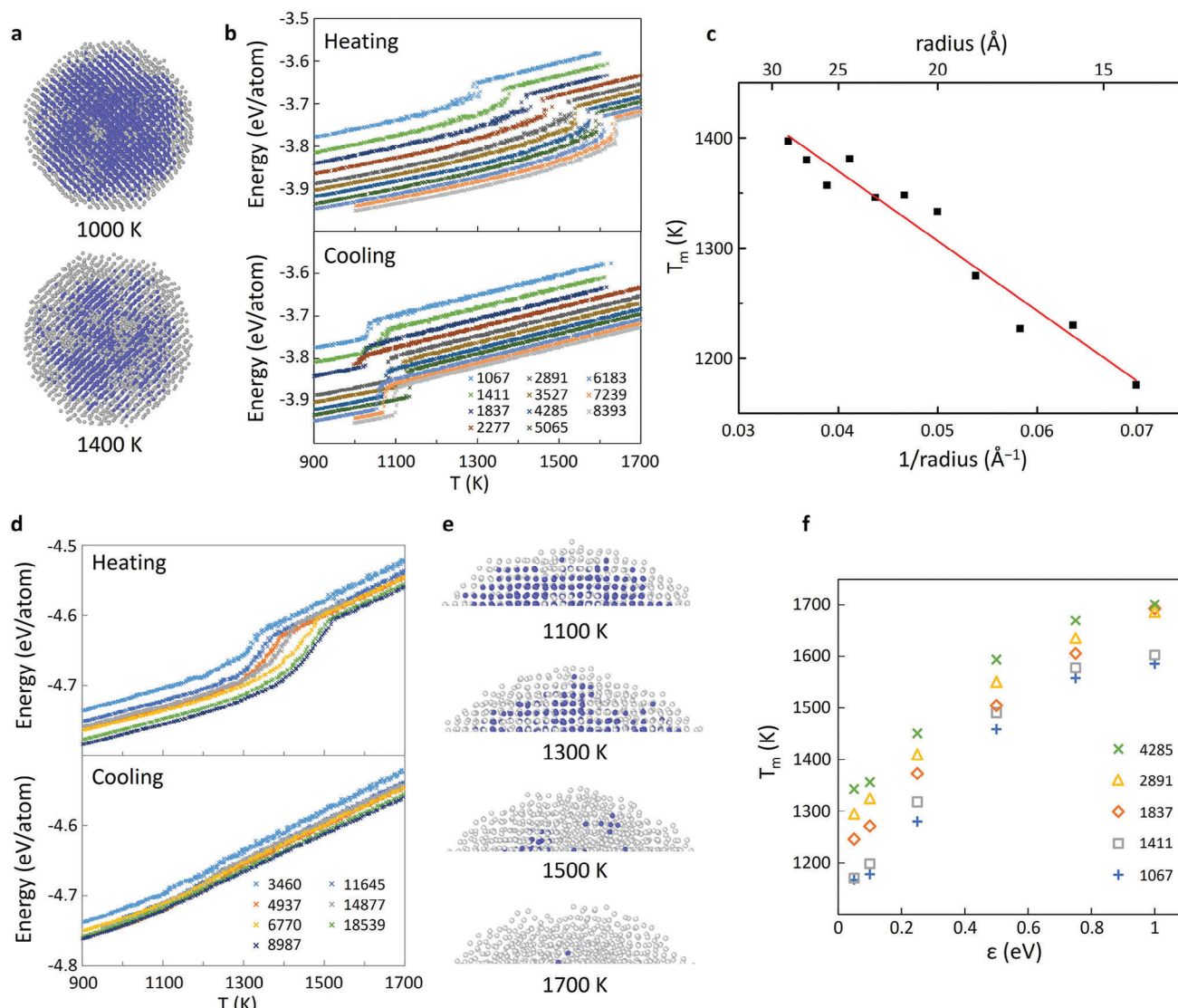


**Figure 5.** a) Snapshots of a heating simulation of a freestanding  $\alpha$ -iron cluster constructed from 8393 atoms. b) Caloric curves calculated from heating and cooling simulations of  $\alpha$ -iron clusters of various sizes. c) Equilibrium melting temperature ( $T_m$ ) versus  $1/\text{radius}$  for  $\alpha$ -Fe clusters with a fit line calculated using Pawlow's formula.<sup>[22]</sup> d) Caloric curves calculated from heating and cooling simulations of  $\text{Fe}_3\text{C}$  clusters of various sizes. e) Snapshots of a heating simulation of  $\alpha$ -Fe cluster consisting of 5065 atoms with a cluster-substrate interaction strength of 1.0 eV. f) Plot of equilibrium melting temperature versus cluster-substrate interaction strength ( $\epsilon$ ) for BCC Fe clusters of various sizes. The numbers in the legends in panels (b), (d), and (f) indicate the number of atoms in the cluster.

temperature (1100 K), the face-centered cubic (FCC) structure transformed instantly to BCC, as expected from the phase diagram.

Simulations of freestanding  $\text{Fe}_3\text{C}$  clusters were carried out using MEAM potentials reported by Liyanage et al.<sup>[23]</sup> In heating simulations, a clear jump in energy was observed in the caloric curves (Figure 5d), corresponding to a melting transition. However, the freezing transition in cooling simulations was less well defined, making it difficult to assign a specific solidification point. This could be due to the metastable nature of the  $\text{Fe}_3\text{C}$  phase, which will decompose into iron and carbon. The only previous simulations of  $\text{Fe}_3\text{C}$  melting and solidification involved a box half-filled with solid  $\text{Fe}_3\text{C}$  atoms and half with liq-

uid atoms.<sup>[21]</sup> This provided a nucleation surface for solidification. In the freestanding  $\text{Fe}_3\text{C}$  clusters, the energy barrier to homogeneous nucleation could be too high, or the rate of nucleation is too slow to be captured on the short timescale of the MD simulation.

The nanoparticles involved in catalytic graphitization are in constant contact with the carbon. Therefore, we also evaluated the impact of particle size on melting point for particles in contact with a substrate. Figure 5e shows a selection of snapshots of a typical simulation, showing the BCC structure of  $\alpha$ -iron (blue atoms) breaking down on melting. Caloric curves were constructed for clusters of a range of sizes and for a range of cluster-substrate interaction strengths. While melting point decreases with



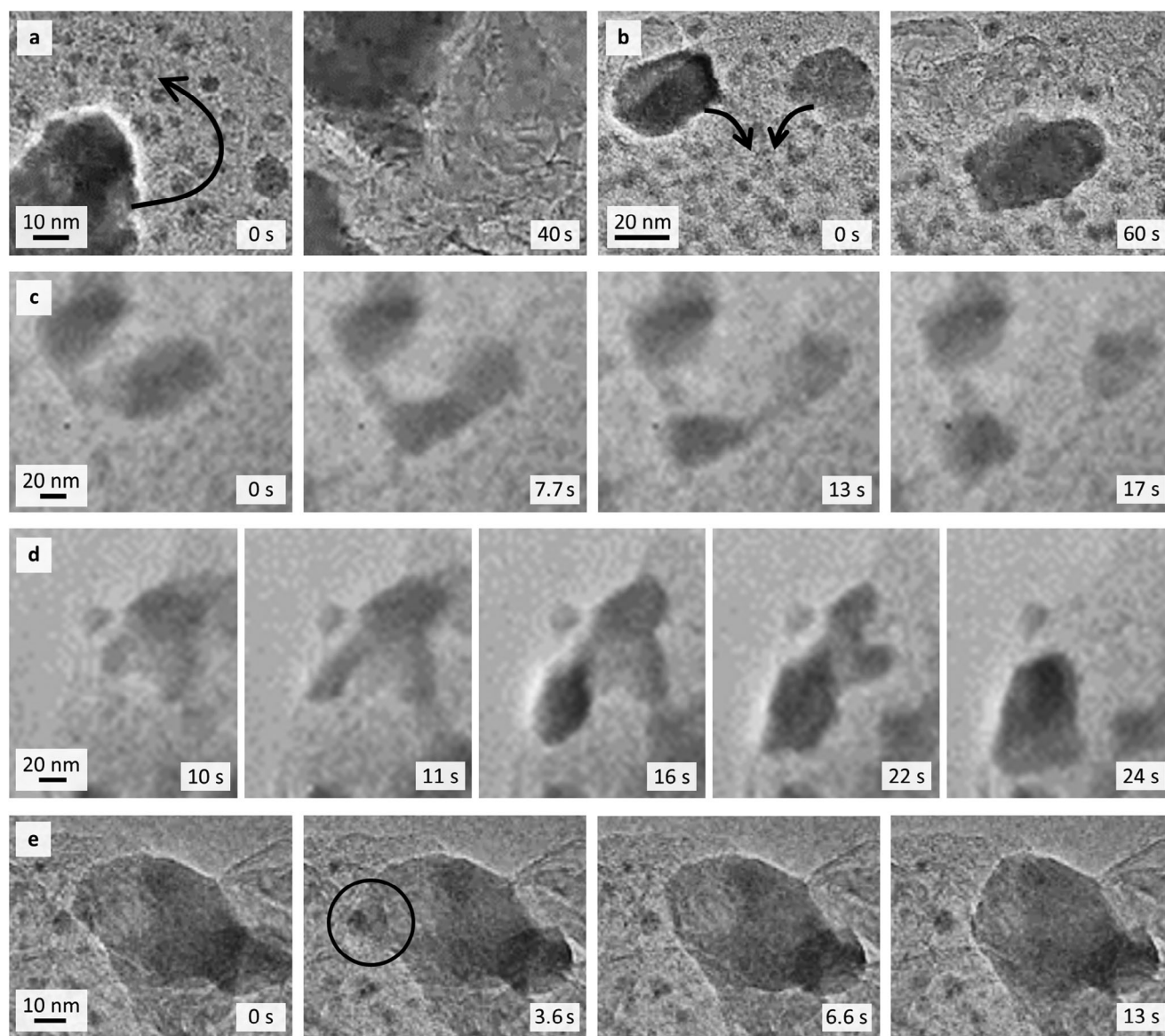


**Figure 6.** Images from in situ TEM footage showing a) a moving particle accumulating smaller Fe-C nanoparticles. b) Two moving particles coalescing. c) A particle dividing. d) A particle appearing to squeeze through a small gap and e) a particle sending out a “tongue” of material before retracting.

decreasing cluster size, it increases with a higher cluster-substrate interaction strength (Figure 5f). This is consistent with the concept of effective radius of curvature, where a particle strongly wetting a surface has a surface curvature equivalent to a much larger particle and displays a melting point closer to that of the equivalent larger particle. Similar simulations for  $\text{Fe}_3\text{C}$  clusters were conducted. Only heating simulations were considered, given the lack of an observable solidification transition in the freestanding clusters. A similar trend was observed, with a larger cluster-substrate interaction strength giving a higher melting point (Figure S11, Supporting Information). All the molecular dynamics simulations together suggest that size effects would not result in a significant melting point depression for either  $\text{Fe}_3\text{C}$  or Fe catalyst particles. This is consistent with our experimental TEM observations.

## 2.4. Insight into the Catalyst Movement

Further insight into the graphitization mechanism can be gained from closer examination of the in situ TEM footage. The moving catalyst particles collect smaller stationary particles (Figure 6a) and merge with other moving particles (Figure 6b) as they travel through the amorphous carbon matrix, resulting in a general increase in size of the particles. The fact that the very small particles are stationary suggests that there may be a critical size that particles need to reach before they become catalytically active and able to move. In some cases, particles split into two smaller particles (Figure 6c). This indicates that the forward driving force for particle movement is very strong. As noted above, many catalysts that appear to be stationary are in fact moving within a confined region, presumably because they have been trapped between

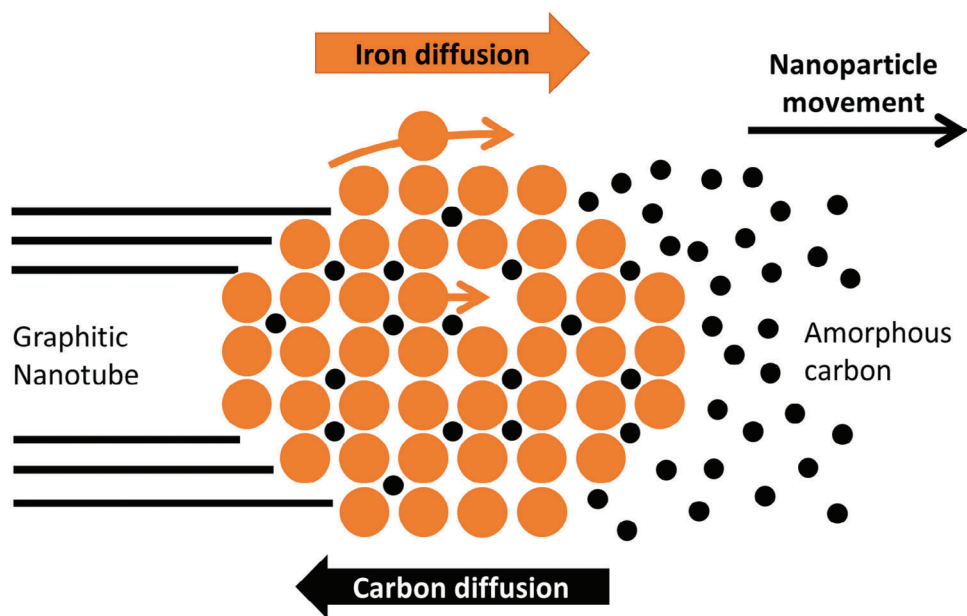


**Figure 7.** Schematic of proposed homogeneous solid-state catalysis mechanism, including (surface and/or vacancy) diffusion of iron through the amorphous carbon matrix and interstitial diffusion of carbon atoms through the iron in the opposite direction, with subsequent precipitation of a graphitic nanotube.

regions of graphitic carbon. In some cases, the catalysts discover small channels of amorphous carbon and will squeeze through narrow gaps to continue graphitization (Figure 6d). This again suggests there is a very strong driving force for catalyst movement. In other cases, catalyst particles send out tongues of catalyst material to consume small pockets of residual amorphous carbon (Figure 6e), again indicating that dissolution of amorphous carbon is energetically favorable.

### 2.5. Mechanism of Iron-Catalyzed Graphitization

The remarkable observation of solid-state homogeneous catalysis can be rationalized by considering atomic diffusion. Atoms diffuse through solids via several mechanisms. In iron or iron carbide, the carbon atoms will be present in the close-packed iron lattice on interstitial sites and will diffuse through the lattice by moving between interstices. Diffusion of carbon in the iron lattice depends on temperature and carbon concentration but is faster in  $\alpha$ -iron ( $D_c \approx 10^{-6} \text{ cm}^2 \text{ s}^{-1}$  at  $800^\circ\text{C}$ ) than  $\gamma$ -iron ( $D_c \approx 10^{-8} \text{ cm}^2 \text{ s}^{-1}$  at  $800^\circ\text{C}$ ) because of the lower density body-centered-cubic structure.<sup>[24]</sup> Diffusion of carbon is slowest in the stoichiometric  $\text{Fe}_3\text{C}$  phase ( $D_c \approx 10^{-10} \text{ cm}^2 \text{ s}^{-1}$  at  $800^\circ\text{C}$ ).<sup>[25]</sup> Diffusion of iron atoms in iron (self-diffusion) occurs by movement of atoms between lattice vacancies. This is by nature a slower process than interstitial carbon diffusion ( $D_c \approx 10^{-12} \text{ cm}^2 \text{ s}^{-1}$  for Fe in  $\alpha$ -iron at  $800^\circ\text{C}$ ),<sup>[26]</sup> but faster at grain boundaries or on surfaces.<sup>[27]</sup> Diffusion of atoms through nanoscale solids can cause rapid structural transformations. An example of this is the diffusion of bismuth atoms outward from a bismuth nanoparticle through a  $\text{Bi}_2\text{O}_3$  shell to form a hollow  $\text{Bi}_2\text{O}_3$  nanoparticle through the Kirkendall Effect.<sup>[28]</sup> The diffusion coefficient of Bi in the  $\text{Bi}_2\text{O}_3$  shell was calculated to be  $0.75 \times$

$10^{-14} \text{ cm}^2 \text{ s}^{-1}$  and the formation of hollow  $\text{Bi}_2\text{O}_3$  nanoparticles from Bi nanoparticles ( $\approx 100 \text{ nm}$  diameter) was completed within 2–5 min. This is a similar timescale to the graphitization process observed in this paper. Self-diffusion of iron (most likely via surface diffusion) is therefore a reasonable mechanism for the movement of the catalyst particle during graphitization (Figure 7).

### 3. Conclusions

Iron-catalyzed graphitization is a fascinating process. A simple and abundant transition metal can convert raw biomass to a dense network of multiwalled carbon nanotubes at moderate temperatures. On a fundamental level, the observation that the graphitization catalyst is crystalline is remarkable and raises the question of what is meant by the word solid. The ordered structure of the crystalline lattice is consistent with microscopic chemical and mechanical definitions of solids.<sup>[29]</sup> Furthermore, the evidence of a melting transition in the DSC well above the graphitization temperature indicates that the catalyst has not undergone a solid-liquid phase transformation when it starts to move. While the observations of the catalyst fit within accepted definitions of solids, the behavior certainly challenges our everyday understanding of solids as rigid materials which retain their shape. This paper also opens up many fascinating research questions. What is the driving force for catalyst movement? Why is the catalyst movement so erratic? Does the nature of the organic precursor impact the way that the catalyst moves? Is  $\text{Fe}_3\text{C}$  or  $\alpha$ -Fe the active catalyst? If we can answer these questions, we may be able to control catalyst movement and use this simple method to produce carbons with tailored graphitic structure and properties. It may even be possible to control the chirality of the resulting nanotubes. Given the importance of carbon in energy technologies,



this would represent a huge leap forward in sustainable materials production.

## 4. Experimental Section

**Iron-Doped Amorphous Carbon Sample Preparation:** Cellulose fibers (C6288) and iron (III) nitrate nonahydrate were sourced from Sigma-Aldrich. 0.27 g (0.00 068 moles) of  $\text{Fe}(\text{NO}_3)_3 \cdot 9\text{H}_2\text{O}$  was dissolved in 15 mL of DI water and the resulting solution added to a beaker containing 5 g of cellulose fibers (powder). The mixture was manually stirred until the solution had been absorbed. The sample was dried in an air oven at 70 °C to give an orange/yellow solid. The sample was pyrolyzed in an alumina boat crucible in a tube furnace to 400 °C under nitrogen. The heating rate was 5 °C min<sup>-1</sup>.

**TEM Measurements:** Small portions of iron-doped amorphous carbon sample (≈50 mg) were dispersed in ethanol (≈1 mL) by sonication for 10 min. One drop of the dispersion was pipetted on to a Protochips Thermal E-chip (E-FHDC). In situ TEM footage was collected on a JEOL JEM-ARM200F equipped with a Schottky field emission gun. The sample was heated at 1 °C min<sup>-1</sup> with a Protochips heating holder, FUSION, inside the microscope. Dark field TEM footage was collected at 900 °C inside the microscope.

**In Situ Synchrotron Powder X-Ray Diffraction:** In situ X-ray diffraction experiments were carried out at the materials science powder diffraction (MSPD) beamline of the ALBA-CELLS synchrotron (Cerdanyola del Vallés, Spain). Beam energy was ≈30 keV (wavelength  $\lambda = 0.4127 \text{ \AA}$  as determined using a Si standard) and scattering was measured in the range ≈1° to ≈60° in 2 $\theta$  using an array of linear position sensitive detectors (Dectris Mythen). Powdered samples were contained in open-ended quartz capillaries (1 mm inner diameter) and held in place using quartz wool. Heating was performed in a capillary flow-cell<sup>[30]</sup> using a hot-air blower (Oxford FMB), while N<sub>2</sub> flowed through the sample at a nominal rate of 20 mL min<sup>-1</sup>, which was controlled at the inlet and monitored at the outlet using mass flow controllers.

The samples had been previously heated ex situ in a laboratory furnace up to 400 °C to release the most volatile products of pyrolysis. During in situ experiments, the samples were heated at 20 °C min<sup>-1</sup> up to 400 °C, then at 5 °C min<sup>-1</sup> up to 800 °C, held at 800 °C for 2 h and then cooled down to 100 °C at a rate of 20 °C min<sup>-1</sup>. Diffraction patterns were measured continuously every minute. Real temperature at the sample was calibrated previously using a K-type thermocouple in place of the sample and later checked by observing several phase transitions.

**TGA/MS:** Thermogravimetric analysis (TGA) coupled with differential scanning calorimetry (DSC) experiments were carried out using a dual system (SDT Q600, Thermal Advantage Instruments). Samples consisting of raw cellulose and cellulose impregnated with  $\text{Fe}(\text{NO}_3)_3$  solution were measured from 100 to 1350 °C using a heating rate of 5 °C min<sup>-1</sup> under flowing Ar at 100 mL min<sup>-1</sup>. An initial mass of ≈10 mg was used, and samples were contained in brand-new alumina pans that were previously washed in 1 M HCl solution to discard the presence of any metal contaminants. The exhaust of the system was connected to a mass spectrometer (GSD 320 Omnistar, Pfeiffer Vacuum) to qualitatively evaluate the composition of the gases evolved during pyrolysis. A secondary electron multiplier detector polarized at 970 V was used, and m/Z ratios of 10 to 50 u.m.a were measured at a scan rate of 200 ms/u.m.a.

**Molecular Dynamics Simulations: Free Standing Clusters:** Clusters of BCC-Fe, FCC-Fe, and Fe<sub>3</sub>C were constructed in LAMMPS using lattice parameters extracted from crystallographic data and a spherical cluster with a certain radius was defined. For pure Fe clusters, the Fe–Fe interactions were modeled using a modified embedded atom model (MEAM) potential reported by Asadi et al.<sup>[20]</sup> For Fe–C clusters, the MEAM potential reported by Liyanage et al. was used to describe the Fe–Fe, Fe–C, and C–C interactions.<sup>[23]</sup>

The classical equations of motion were integrated using a timestep of 2.0 fs and the temperature was controlled using the Langevin thermostat. Periodic boundary conditions were employed in the x, y, and z directions. The clusters were initially annealed at the starting temperature for 10 ns

before the start of a simulation. Heating and cooling simulations were then carried out at a rate of 16 K ns<sup>-1</sup> and statistical averages were generated. Trajectories were visualized using OVITO.

**Molecular Dynamics Simulations: Substrate-Supported Fe Clusters:** The same procedure was carried out to construct clusters with a BCC-Fe, FCC-Fe, or Fe<sub>3</sub>C structure and the same Asadi and Liyanage potentials were used to describe the interactions within the cluster. A fixed wall substrate was introduced along the z-plane of the simulation box and periodic boundary conditions were only employed in the x and y directions. The cluster–substrate interaction was described using a Lennard–Jones 12–6 potential. The distance of closest approach ( $\sigma$ ) in the Lennard–Jones potential was fixed at 2.91 Å. The well depth ( $\epsilon$ ) was varied from 0.05 to 1.0 eV to model the variable strength of interaction between the clusters and the substrate.

The classical equations of motion were also integrated using a timestep of 2.0 fs. The angular momentum of the clusters in the x–y plane were fixed at each step to prevent movement of the cluster along the substrate during the simulation. To reduce computational cost, only the atoms within the nanoparticles were heated in the NVE ensemble using a Langevin thermostat. The clusters were initially annealed at a fixed distance of 2 $\sigma$  from the substrate at the starting temperature of the simulation for 10 ns. The cluster was then relaxed at the initial temperature for 5 ns to allow for the cluster to wet onto the substrate. Heating and cooling procedures were then carried out as with the freestanding clusters.

**Molecular Dynamics: Calculation of Melting/Freezing Transitions:** The melting/freezing transition of the clusters was characterized by plotting caloric curves (E(T) vs T). The phase transition temperature was also characterized from the heat capacities, which were calculated from the fluctuations of energy using Equation (1)

$$C_v = \frac{\langle E^2 \rangle - \langle E \rangle^2}{k_B T^2} \quad (1)$$

In general, the combination of the two methods were used to confirm the temperature at which melting or freezing occurred. To avoid effects of superheating/supercooling, melting, and freezing simulations were run for each cluster at the same heating/cooling rate. For most of the clusters tested, there was some level of hysteresis, where the freezing transition occurs at a lower temperature than the melt. This is a common phenomenon due to the fast heating and cooling rates required for MD and were accounted for by applying Equation (2) to calculate an equilibrium melting temperature,  $T_m$

$$T_m = T_c^+ - \sqrt{T_c^+ T_c^-} + T_c^- \quad (2)$$

where  $T_c^+ = T$  of melting transition and  $T_c^- = T$  of freezing transition.

## Supporting Information

Supporting Information is available from the Wiley Online Library or from the author.

## Acknowledgements

Z.S. acknowledged the Leverhulme Trust (No. RPG-2020-076) and the University of Birmingham for funding. J.R.-R. acknowledged funding from the Spanish Ministry of Science, Innovation and Universities (Grant No. PID2019-107019RB-I00) and from the Junta de Andalucía regional government (Grant Nos. P20-01186 and US-1380856, with funds from FEDER). In situ x-ray diffraction experiments were performed at the MSPD beamline at ALBA synchrotron with the collaboration of ALBA staff (Experiment No. 2021024916).

## Conflict of Interest

The authors declare no conflict of interest.

## Data Availability Statement

The data that support the findings of this study are available from the corresponding author upon reasonable request.

## Keywords

graphitization, homogeneous solid-state catalysis, nanotube

Received: March 21, 2024  
Revised: June 24, 2024  
Published online: July 16, 2024

- [1] L. Güniat, P. Caroff, A. Fontcuberta i Morral, *Chem. Rev.* **2019**, *119*, 8958.
- [2] J. Pang, A. Bachmatiuk, I. Ibrahim, L. Fu, D. Placha, G. S. Martynkova, B. Trzebicka, T. Gemming, J. Eckert, M. H. Rummeli, *J. Mater. Sci.* **2016**, *51*, 640.
- [3] K. W. Kolasinski, *Curr. Opin. Solid State Mater. Sci.* **2006**, *10*, 182.
- [4] R. D. Hunter, J. Ramírez-Rico, Z. Schnepp, *J. Mater. Chem. A* **2022**, *10*, 4489.
- [5] R. D. Hunter, J. L. Rowlandson, G. J. Smales, B. R. Pauw, V. P. Ting, A. Kulak, Z. Schnepp, *Mater. Adv.* **2020**, *1*, 3281.
- [6] S. Glatzel, Z. Schnepp, C. Giordano, *Angew. Chem., Int. Ed.* **2013**, *52*, 2355.
- [7] O. P. Krivoruchko, V. I. Zaikovskii, *Mendeleev Commun.* **1998**, *8*, 97.
- [8] O. P. Krivoruchko, N. I. Maksimova, V. I. Zaikovskii, A. N. Salanov, *Carbon* **2000**, *38*, 1075.
- [9] H. Rastegar, M. Bavand-vandchali, A. Nemati, F. Golestani-Fard, *Phys. E* **2018**, *101*, 50.
- [10] E. Thompson, A. E. Danks, L. Bourgeois, Z. Schnepp, *Green Chem.* **2015**, *17*, 551.
- [11] N. D. Klein, K. R. Hurley, Z. V. Feng, C. L. Haynes, *Anal. Chem.* **2015**, *87*, 4356.
- [12] L. Wang, J. Teng, P. Liu, A. Hirata, E. Ma, Z. Zhang, M. Chen, X. Han, *Nat. Commun.* **2014**, *5*, 4402.
- [13] Y. Wang, L. Qiu, L. Zhang, D.-M. Tang, R. Ma, C.-L. Ren, F. Ding, C. Liu, H.-M. Cheng, *Sci. Adv.* **2022**, *8*, eabo5686.
- [14] M. S. Chambers, R. D. Hunter, M. J. Hollamby, B. R. Pauw, A. J. Smith, T. Snow, A. E. Danks, Z. Schnepp, *Inorg. Chem.* **2022**, *61*, 6742.
- [15] J. Chipman, *Metall. Trans.* **1972**, *3*, 55.
- [16] Z. He, J.-L. Maurice, A. Gohier, C. S. Lee, D. Pribat, C. S. Cojocaru, *Chem. Mater.* **2011**, *23*, 5379.
- [17] H. K. D. H. Bhadeshia, *J. Mater. Sci.* **2004**, *39*, 3949.
- [18] F. Ding, A. Rosén, S. Curtarolo, K. Bolton, *Appl. Phys. Lett.* **2006**, *88*, 133110.
- [19] V. Rosato, M. Guillope, B. Legrand, *Philos. Mag. A* **1989**, *59*, 321.
- [20] E. Asadi, M. A. Zaeem, S. Nouranian, M. I. Baskes, *Phys. Rev. B* **2015**, *91*, 024105.
- [21] S. N. Luo, A. Strachan, D. C. Swift, *J. Chem. Phys.* **2004**, *120*, 11640.
- [22] P. Pawlow, *Z. Phys. Chem.* **1909**, *65*, 1.
- [23] L. S. I. Liyanage, S.-G. Kim, J. Houze, S. Kim, M. A. Tschopp, M. I. Baskes, M. F. Horstemeyer, *Phys. Rev. B* **2014**, *89*, 094102.
- [24] J. Cermak, L. Kral, *J. Alloys Compd.* **2014**, *586*, 129.
- [25] A. Schneider, G. Inden, *Calphad* **2007**, *31*, 141.
- [26] Y. Iijima, K. Kimura, K. Hirano, *Acta Metall.* **1988**, *36*, 2811.
- [27] A. Inoue, H. Nitta, Y. Iijima, *Acta Mater.* **2007**, *55*, 5910.
- [28] K.-Y. Niu, J. Park, H. Zheng, A. P. Alivisatos, *Nano Lett.* **2013**, *13*, 5715.
- [29] S. Alexander, *Physica A* **1998**, *249*, 266.
- [30] P. J. Chupas, K. W. Chapman, C. Kurtz, J. C. Hanson, P. L. Lee, C. P. A. Grey, *J. Appl. Crystallogr.* **2008**, *41*, 822.